The Astrophysical Journal, 884:131 (9pp), 2019 October 20 https://doi.org/10.3847/1538-4357/ab4270

Large-amplitude Quasiperiodic Pulsations as Evidence of Impulsive Heating in Hot Transient Loop Systems Detected in the EUV with *SDO*/AIA

Fabio Reale[1,2], Paola Testa[3], Antonino Petralia[2], and Dmitrii Y. Kolotkov[4]
[1] Dipartimento di Fisica & Chimica, Università di Palermo, Piazza del Parlamento 1, I-90134 Palermo, Italy; fabio.reale@unipa.it
[2] INAF-Osservatorio Astronomico di Palermo, Piazza del Parlamento 1, I-90134 Palermo, Italy
[3] Harvard—Smithsonian Center for Astrophysics, 60 Garden Street, Cambridge, MA 02138, USA
[4] Centre for Fusion, Space and Astrophysics, Department of Physics, University of Warwick, Coventry CV4 7AL, UK
Received 2019 April 16; revised 2019 September 4; accepted 2019 September 5; published 2019 October 18

Abstract

Short heat pulses can trigger plasma pressure fronts inside closed magnetic tubes in the corona. The alternation of condensations and rarefactions from the pressure modes drive large-amplitude pulsations in the plasma emission. Here we show the detection of such pulsations along magnetic tubes that brighten transiently in the hot 94 Å EUV channel of the *Solar Dynamics Observatory*/AIA. The pulsations are consistent with those predicted by hydrodynamic loop modeling, and confirm pulsed heating in the loop system. The comparison of observations and model provides constraints on the heat deposition: a good agreement requires loop twisting and pulses deposited close to the footpoints with a duration of 0.5 minutes in one loop, and deposited in the corona with a duration of 2.5 minutes in another loop of the same loop system.

Key words: Sun: activity – Sun: corona

1. Introduction

The diagnostic of coronal heating both in quiescent and flaring conditions is an important issue (e.g., Klimchuk 2006; Reale 2014). Several mechanisms have been invoked, from waves propagating upwards from the chromosphere (e.g., Ionson 1978; Ofman et al. 1998; McIntosh et al. 2011; van Ballegooijen et al. 2011; Morton et al. 2019) to small-scale reconnection in the corona (e.g., Parker 1988; Kopp & Poletto 1993; Vekstein & Katsukawa 2000; Hood et al. 2009; Priest 2011; Cargill et al. 2015), but unique signatures are difficult to find. Indirect evidence can therefore be very important.

Flare-like rapid enhancements of the coronal emission are often observed to be accompanied by quasiperiodic pulsations (QPPs), manifested as relatively short-lived modulations of the light curves by wave and oscillatory processes in active regions (see reviews by Nakariakov & Melnikov 2009; Van Doorsselaere et al. 2016). Such pulsations are seen to be omnipresent in both solar (e.g., Kupriyanova et al. 2010; Simões et al. 2015; Inglis et al. 2016) and stellar (e.g., Cho et al. 2016; Pugh et al. 2016; Doyle et al. 2018) emission throughout the whole electromagnetic spectrum and in both thermal and nonthermal emissions. One can distinguish at least three groups of potential physical mechanisms which could be responsible for the observed QPP (see McLaughlin et al. 2018 for the most recent detailed review of the QPP mechanisms): direct modulation of the emitting plasma parameters by eigen magnetohydrodynamic (MHD) modes of an oscillating loop (e.g., Nakariakov & Verwichte 2005; De Moortel & Nakariakov 2012), periodic triggering of the energy release processes by external MHD oscillations (e.g., Nakariakov et al. 2006; McLaughlin et al. 2011), and regimes of repetitive energy releases ongoing in a self-oscillatory manner (e.g., Kliem et al. 2000; Murray et al. 2009; Thurgood et al. 2019). Rapidly decaying pulsations detected in thermal emission, with periods of several minutes and with relatively small amplitudes ($\leqslant$10%) were generally interpreted in terms of compressive slow magnetoacoustic waves (e.g., Kim et al. 2012; Kolotkov et al. 2018), with exceptions (e.g., Svestka 1994). Those waves have been detected in hotter UV and EUV channels, e.g., in flare-like events in Fe XIX 1118 Å and Fe XXI 1354 Å spectral line profiles with the SUMER spectrograph on *SOHO* (Wang 2011), and more recently, in the *Solar Dynamics Observatory* (*SDO*)/AIA 131 and 94 Å channels (Kumar et al. 2013, 2015; Wang et al. 2015), and they are typically interpreted as magnetoacoustic wave fronts that evolve into slow standing waves. Slow waves, modulating the observed thermal emission intensity via density and temperature perturbations, have been studied extensively through hydrodynamic and MHD modeling of plasma inside closed magnetic tubes. Much attention has been devoted to wave generation by upflows (Selwa et al. 2005; Fang et al. 2015) or velocity drivers (Wang et al. 2013) and damping and dissipation of harmonics through thermal conduction and viscosity (Ofman & Wang 2002; De Moortel & Hood 2003; Wang et al. 2018), gravitational stratification and magnetic field line divergence (De Moortel & Hood 2004), nonlinear damping (Verwichte et al. 2008; Ruderman 2013), mode coupling (De Moortel et al. 2004), and their relative efficiency in specific physical conditions. More recent works by Wang et al. (2015) and Wang et al. (2018) showed the need for the modification of the thermal conduction and viscosity coefficients from their standard estimates (suppressed or enhanced by up to an order of magnitude) in order to match the observational properties of slow waves. This suggests that neither conduction nor viscosity is always a sufficient mechanism for the interpretation of the observed behavior of slow waves, and additional physical effects should be taken into account. For example, a wave-induced perturbation of the thermodynamical equilibrium between some unspecified plasma heating and radiative cooling was shown to strongly affect the dynamics of slow waves, leading to their enhanced damping or amplification (Kumar et al. 2016; Nakariakov et al. 2017). Moreover, recent statistical study of slow wave properties (Nakariakov et al. 2019) revealed scaling laws between the oscillation periods, damping times, amplitudes, and the loop temperature, that require further theoretical interpretation. In

particular, the damping of spatial harmonics of the sloshing (i.e., propagating and reflecting slow oscillations) was observed to be different to that in the standing slow waves. As such, slow coronal magnetoacoustic waves and a related modulation of the coronal emission in the form of QPP remain an actively developing and interesting research avenue, providing important insights into the field of MHD coronal seismology, contributing, in particular, to probing coronal plasma transport coefficients and constraining properties of the coronal heating function.

For example, an advanced recent, time-dependent hydrodynamic loop modeling that includes all relevant physical effects (gravity, thermal conduction, radiative losses, and plasma heating) and a highly stratified atmosphere from the chromosphere to the corona shows that short heat pulses can easily trigger significant pressure fronts that move back and forth along a loop and settle down to low-order standing modes with long wavelength (Reale 2016). The heat pulses must be so short-lasting that the pressure does not have enough time to reach an equilibrium inside the loop during the heating phase and the sudden switch off creates a localized pressure drop which drives the fronts. The efficient thermal conduction smooths out temperature perturbations in the hot corona, but the pressure fronts drive strong density fronts that periodically accumulate when they are reflected and in turn determine strong alternating excesses and reductions of emission measure (EM) which modulate the light curves with long-period and large-amplitude pulsations. Hydrodynamic loop modeling has been able to reproduce long flares showing pulsations with periods of hours and amplitudes of $\sim$20% observed in the X-rays from protostars in the Orion region (Reale et al. 2018).

On the Sun, bright UV spots detected in active regions with the *Interface Region Imaging Spectrograph* (*IRIS*) at the footpoints of transient hot loops could be explained with the presence of pulsed energy release in the corona (Testa et al. 2014; Polito et al. 2018; P. Testa et al. 2019, in preparation). Detected Doppler shifts were modeled with the release of nonthermal electron beams. It has been shown that these hot spots are at the footpoints of coronal loops that brighten for a few minutes in the hottest EUV *SDO*/AIA channels, thus involving plasma heated to more than 10 MK (Reale et al. 2019).

In these coronal loops we may detect pulsations. Full-disk monitoring with the Atmospheric Imaging Assembly (AIA) on board the *SDO* allows for full temporal and spatial coverage. The image cadence ($\sim$10 s) is sufficiently high to resolve pulsations with periods larger than $\sim$1 minute, which might be expected for magnetic arches longer than 10 Mm. The detection might be nontrivial, mostly because the regions contain several bright loops that intersect along the line of sight.

Here we describe the detection of pulsations from *SDO*/AIA images in regions with *IRIS* hot spots and we show their consistency with predictions by hydrodynamic loop modeling. We demonstrate that the observed QPP could be caused by a slow wave evolving in a closed magnetic loop and triggered by a short-time heating pulse deposited at the loop footpoints and in the corona. For the first time we link the observed properties of QPP with the properties of the underlying heating process, suggesting a new way of exploiting the QPP observed in the thermal emission for the diagnostics of the coronal heating function.

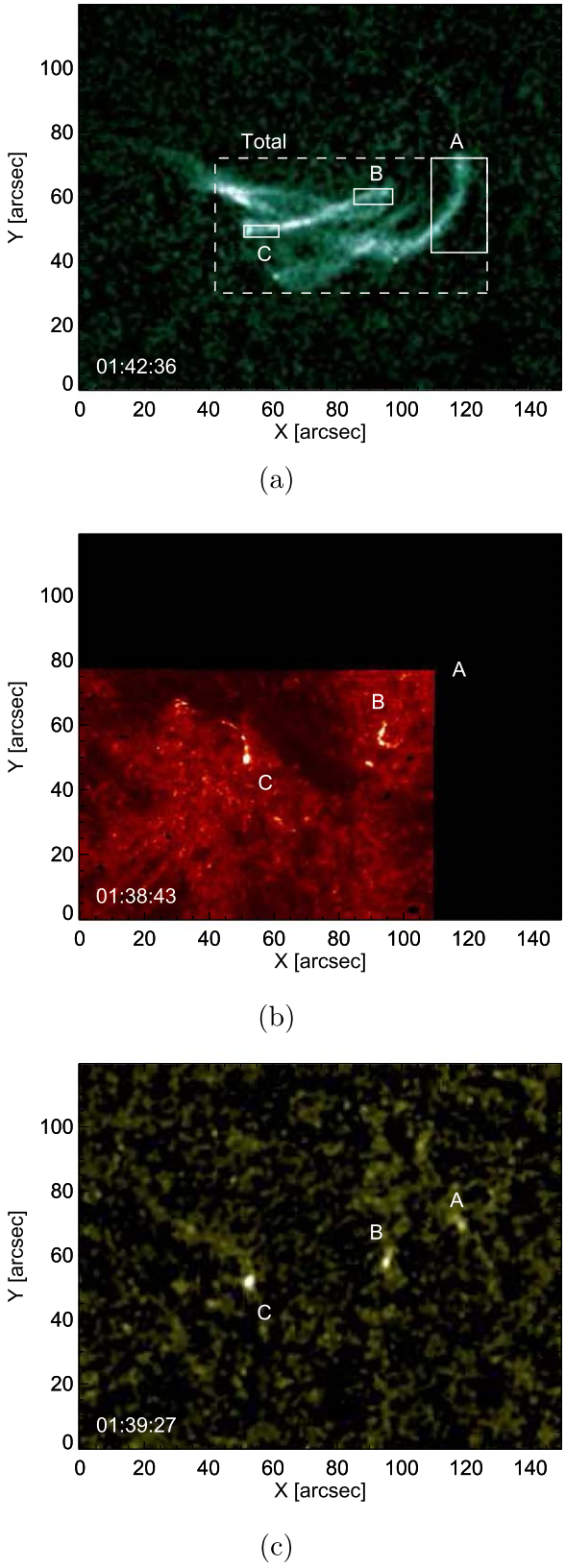

Figure 1. (a) Loop system observed on 2015 November 12 in the AIA 94 Å channel. An image just before the brightening (1:37:12 UT) was subtracted. Light curves in Figure 2 were extracted from the boxes (Total, A, B, and C). (b) Same region observed with *IRIS* in the Si IV 1402 Å line. The position of boxes A, B, and C is marked. (c) Same as (b) but in the AIA 1600 Å channel.

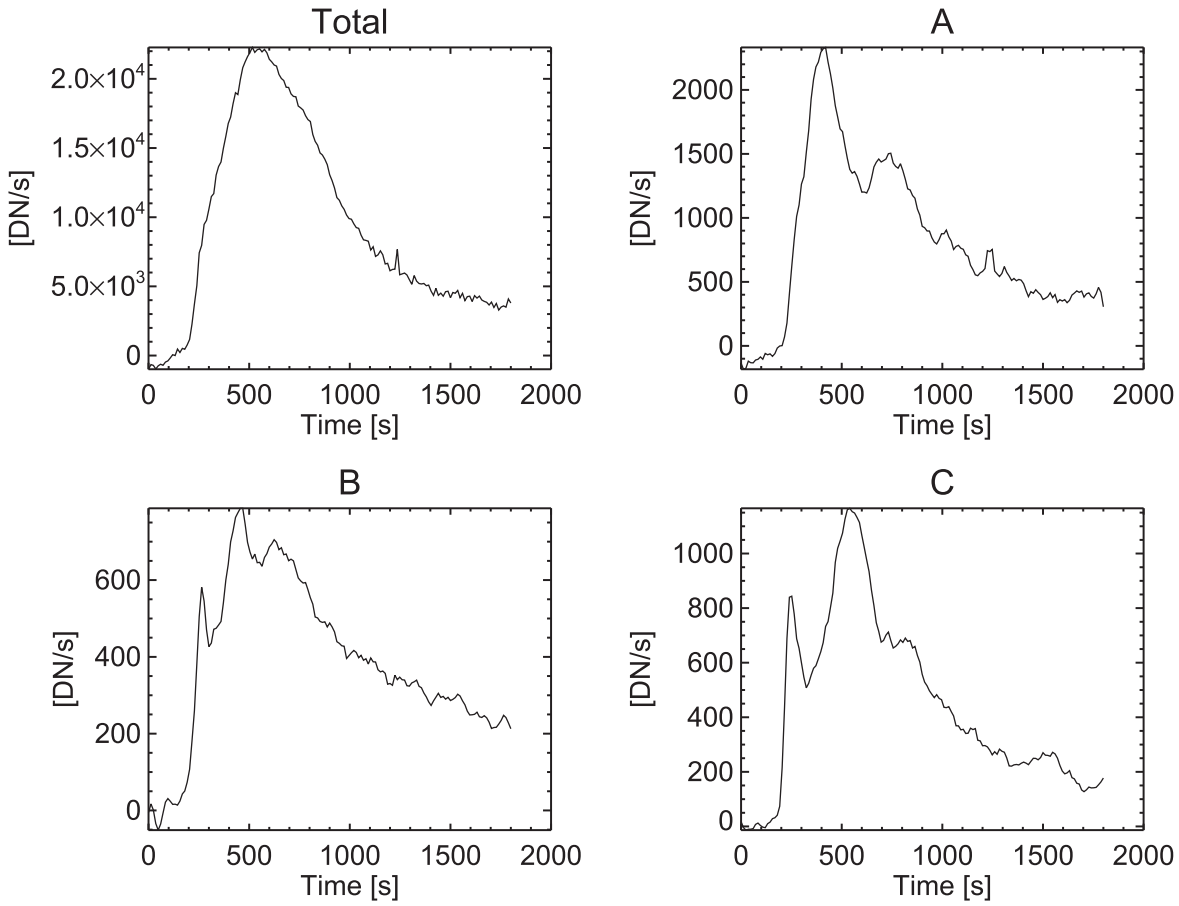

Figure 2. Light curves from the boxes in Figure 1 (time since 01:35 UT).

2. Data Analysis and Modeling

2.1. Observation

We consider loops in an active region observed in the EUV with the AIA (Lemen et al. 2012) on board the *SDO* on 2015 November 12 starting at 1:35 UT and studied also in Reale et al. (2019). The center of the field of view is $XY = [-117\farcs2, -329\farcs6]$. The loops brighten in the 131 Å channel for an amount of time that is too short to show a meaningful pulsation trend (as confirmed by hydrodynamic simulations), so here we focus on the 94 Å channel which includes a highly ionized Fe XVIII line, most sensitive to plasma at temperatures in the range 6–8 MK (Testa & Reale 2012; Boerner et al. 2014). The data processing and analysis is the same as in Reale et al. (2019). The images have been preprocessed with the standard AIA software procedure and coaligned, and we subtract the image just before the brightening of the hot structures (1:37.12 UT). The data set consists of 205 images with an average cadence of 12 s in a total time lapse of 30 minutes, between 01:35 and 02:05 UT, in which the subtracted image is not too far in time.

We analyze the emission from the brightening region in Figure 1(a), and in particular three boxes A, B, and C. The boxes are chosen so as to avoid bright overlapping structures. Box A is taken along a long coronal arch, whose distance between the footpoints is ∼57 Mm, for a maximum total length ∼90 Mm if the loop were semicircular (Reale et al. 2019). Boxes B and C are at the extreme of a shorter transversal structure, whose distance between the footpoints is ∼32 Mm, for a possible maximum length 50 Mm (Reale et al. 2019). In Figures 1(b) and (c) the same region imaged by *IRIS* in the Si IV 1402 Å line and AIA 1600 Å channel, respectively, shows bright spots at the footpoints of both loops.

Figure 2 shows the light curves related to this region in the 94 Å channel after background subtraction, over ∼30 minutes. The total light curve is integrated on the region which contains the loop brightening in this channel and shows a smooth flare-like evolution with a sharp rise, a well-defined peak approximately 5 minutes after the brightening starts and a more gradual decay. This light curve envelopes the others.

The light curves taken in the boxes are significantly different from the total one and share a common feature: all of them show well-defined large-amplitude pulsations. The light curve in box A shows a first high peak at time $t \approx 550$ s, rapidly decaying to a second smaller and smoother one ($t \approx 900$ s), and a third barely visible one. Both boxes B and C share another common feature: an initial similar and almost simultaneous ($t \approx 400$ s) spike. This spike is followed by a peak similar to the peak in box A and by a third bump similar to the second bump in box A. The amplitude of the main pulsations is 20%–40% of the total signal. The separation in time between the peaks, which can be taken as the period of the pulsations, is approximately 300 s for box A, 200 s for box B, and 250–300 s for box C. Pulsations are not detected everywhere in the region, mostly because different structures overlap along the line of sight.

The oscillations are also evident in the temporal evolution of the differential emission measure (DEM), which describes the

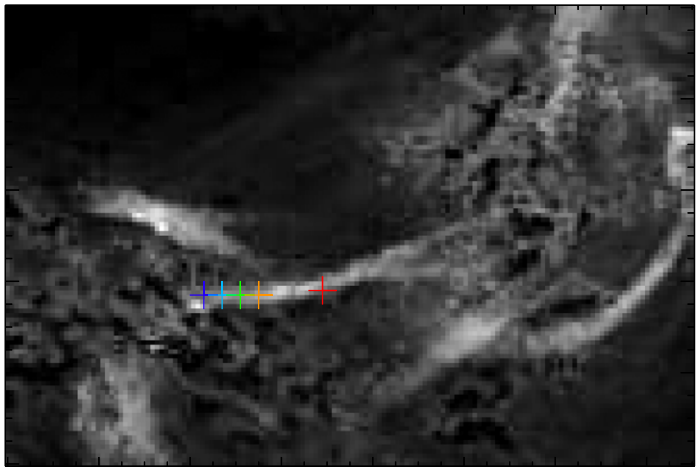

(a)

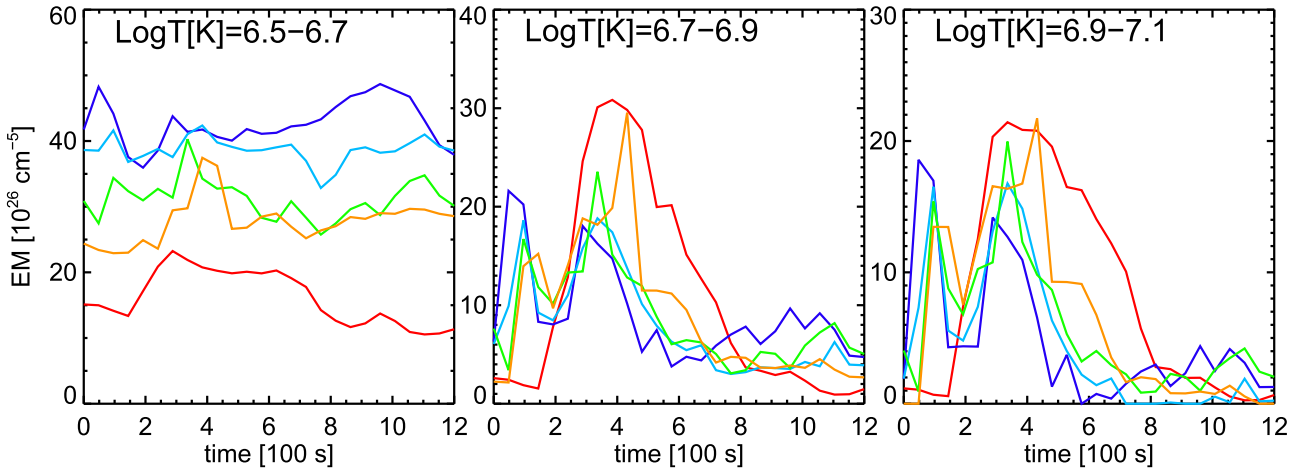

(b)

Figure 3. (a) Map of emission measure in the 6.7–6.9 $\log T$ [K] bin, at 01:41:54 UT. Four locations along one of the pulse-heated loops are marked (colored crosses). (b) Emission measure in three temperature bins (increasing from left to right, as labeled in each panel) vs. time for the four locations in panel (a) with corresponding colors (blue to red, from the loop footpoints to larger heights along the loop). The reference time ($t = 0$) is 01:37:54 UT.

temperature distribution of the coronal plasma along the line of sight. As detailed in a companion paper (Reale et al. 2019), we applied the inversion method by Cheung et al. (2015) to the timeseries of the six coronal AIA passbands (94, 131, 171, 193, 211, and 335 Å) and obtained the DEM in each AIA pixel (no background subtraction is applied here). Figure 3 shows the map of EM distribution in the 6.7–6.9 log $T[K]$ bin, at 01:41:54 UT, and the temporal evolution of the EM in three increasing-temperature bins, for four different locations along a heated loop (corresponding to box C in Figure 1). At high temperatures ($\log T$ [K] $\gtrsim 6.7$) the EM versus time shows pulsations. Excluding the curve for the point close to the apex (red) where other structures clearly overlap along the line of sight, we notice that the first pulsation shifts in time from the footpoint (blue) toward the apex (orange) by about 100 s (see Section 3).

2.2. Modeling

We now show that pulsations similar to the observed ones are reproduced by hydrodynamic modeling of pulse-heated loops as in Reale (2016). We consider a standard loop model in the infinite magnetic field approximation, which describes the time-dependent hydrodynamics of a compressible plasma confined in a closed coronal loop anchored to the photosphere (Peres et al. 1982; Betta et al. 1997; Reale 2016). The one-dimensional time-dependent hydrodynamic equations include the effect of gravity (for a curved flux tube), thermal conduction and compression viscosity (Spitzer 1962), radiative losses for an optically thin plasma, and an external heating input. Under this approximation, the excited slow wave propagates strictly along the ambient magnetic field of an infinite strength, thus not perturbing the field and at the speed independent of it (Goedbloed & Poedts 2004; Priest 2014). The model loop is assumed symmetric with respect to the apex.

Figure 4(a) shows results of modeling of a loop symmetric with respect to its apex, with a half-length $L = 60$ Mm and heated by a single energy pulse with a duration of $\tau_H = 150$ s, an intensity of 0.2 erg cm^{-3} s^{-1} and distributed uniformly along the loop. The total energy flux is 2.4×10^9 erg cm^{-2} s^{-1}. The loop is assumed initially at a maximum temperature of $\sim$1.5 MK. Details about hydrodynamic loop modeling can be found in

Reale (2016) and references therein. The figure includes the evolution of the average temperature, density, and velocity in the lower loop segment, 30 Mm long, roughly corresponding to the one enclosed in box A of Figure 1. The panels show the typical flare-like evolution with a very steep rise of the temperature ~12 MK, and a more gradual rise of the density, due to plasma evaporation from the chromosphere (e.g., Bradshaw & Cargill 2013; Reale 2014), to values $\sim 10^{10}$ cm^{-3}. After the heat pulse stops the temperature decreases very rapidly, and the density much more gradually, as expected (e.g., Bradshaw & Cargill 2010; Reale 2014). From the maximum temperature the condition (Reale 2016):

$$\tau_H < \tau_s \sim 5\frac{L_{\rm Mm}}{\sqrt{0.1\ T_{\rm MK}}} \approx 245\ {\rm s} \quad (1)$$

(where τ_s is the return sound crossing time along the model half-loop, assuming a polytropic index $\gamma \sim 1$) on the duration of the heat pulse confirms that the pulse is able to trigger pulsations inside the loop, which are clearly visible in the density of Figure 4(a). The three main pulsations are included in the time range 500–1500 s, and the period is therefore ~300–350 s. The corresponding speed of the twin wave fronts is ~350–400 km s^{-1}. If we assume wave fronts at the sound speed of a fully ionized plasma $c_s = \sqrt{2\gamma k_B T/m}$, where k_B is the Boltzmann constant and m is the average ion mass, we can make a check of consistency about the temperature T of the medium in which they propagate, under an assumption of the polytropic index γ.

We can estimate the polytropic index γ in our modeling results using the technique previously applied to a number of real observational data sets (see, e.g., Van Doorsselaere et al. 2011; Wang et al. 2015). It allows one to estimate γ as

$$\gamma = \frac{A_T(t)}{A_n(t)} + 1, \quad (2)$$

where $A_T(t)$ and $A_n(t)$ are the instantaneous relative amplitudes of the temperature and density variations, respectively, normalized to their corresponding trends $T_0(t)$ and $n_0(t)$ (see Figure 4). We determine $A_T(t)$ and $A_n(t)$ using the Hilbert transform of the corresponding temperature and density variations shown in Figure 5. For both loop models, the obtained values of the polytropic index γ are seen to vary irregularly being about 1.2 (at the initial phase of the loop evolution with $T > 8$ MK), and from about 1.2 to approximately 5/3 (for the stage of a rapid cooling from 8 to 6 MK), and up to 2 and higher for later times ($T < 5.5$ MK). In order to interpret such a behavior of γ, we point out that the derivation of Equation (2) is based on the polytropic assumption, i.e., $p = K\rho^\gamma$ with small perturbations, independent of the wave dissipation assumption, and that the estimate of the polytropic index using Equation (2) includes all nonadiabatic thermohydrodynamic effects, that is why the measured values are beyond the expected range from thermal conduction alone (where $\gamma = 1$–$5/3$) (see Equation (5) in Wang et al. 2015). For example, the wave-induced imbalance between heating and cooling processes, both present in our model, could also lead to substantial modifications of γ (Zavershinskii et al. 2019). Nevertheless, at the initial stage of the loop evolution, the detected values of $\gamma \approx 1.2$ are consistent with the dominant thermal conduction in the loop evolution and support the assumption of an approximately isothermal loop.

If we consider γ increasing from ~1.2 to ~3, we derive a temperature decreasing from $T \sim 11$ MK to $T \sim 4$ MK, broadly consistent with the temperature trend shown in Figure 4(a). Figure 4(a) shows also a very high speed, up to ~500 km s^{-1}, of the initial evaporation front, which decreases below 100 km s^{-1} already within ~300 s.

The bottom panel of Figure 4(a) shows the light curve synthesized from the model in the AIA 94 Å channel with the usual assumption on the radiative losses from an optically thin plasma and from the standard temperature-dependent channel sensitivity function, and the observed one for comparison. Reale (2016) reports on the emission in the same channel but for a shorter loop ($L = 25$ Mm). The synthetic light curve clearly shows the expected pulsations. The light curve shows a good agreement with that measured in box A of Figure 1: both of them show a first higher peak and a second lower one, approximately with the same ratio of intensity, i.e., a similar pulsation amplitude. The period is also similar. According to the model, the first larger bump is due to a combination of the density pulsation and of the rapid cooling across the channel temperature sensitivity range (Figure 4(a)). The small bump at time $t \sim 400$ s is only barely visible in the light curve of box A, possibly because of data noise.

This light curve shows qualitative differences from those in boxes B and C, and, in particular, it is unable to reproduce the initial spike. Another hydrodynamic simulation provides a better agreement with the light curves in boxes B and C.

Figure 4(b) shows results from a model loop with half-length $L = 40$ Mm. Twin heat pulses with a duration of $\tau_H = 30$ s are deposited symmetrically at the loop footpoints, as Gaussian functions with $\sigma = 1$ Mm at a height of 3 Mm from each footpoint and with an intensity of 20 erg cm^{-3} s^{-1}, corresponding to a total flux of $\approx 10^{10}$ erg cm^{-2} s^{-1}. In this case, the pulse duration threshold is $\tau_H < 160$ s, so pulsations are triggered, and we see them again clearly in the density. Here the quantities are averaged over the lower 20 Mm of the loop, roughly corresponding to boxes B and C in Figure 1. Although overall similar, the evolution shows some differences from the previous model. The larger energy input drives a more effective plasma evaporation to a higher density ($\sim 1.3 \times 10^{10}$ cm^{-3}) and speed (~700 km s^{-1}). The shorter loop corresponds to a faster evolution and to a shorter period of the pulsations (~200 s), with a corresponding wavefront speed of ~400 km s^{-1} (Figure 4(b)). For this model we derive similar values of the sound speed and the γ index as for the previous model (see Figure 5). Another distinctive feature is the initial density spike, followed by smoother pulsations. This is also due to the more effective initial evaporation front driven by this more concentrated heat pulse located much closer to the chromosphere.

The bottom panel of Figure 4(b)) shows the light curve in the 94 Å channel from the loop segment of 20 Mm of this other simulation, and the one observed in box B for comparison. The light curve is a very good match to that in box B if we add an offset of ~50% of the maximum model emission. The initial spike is similar to those in the light curves of boxes B and C (Figure 2). The next two pulsations are also very similar to those observed after the spike in the boxes. The oscillation period is around 200 s. We conclude that the presence of the spike is a signature of heat pulses concentrated at the

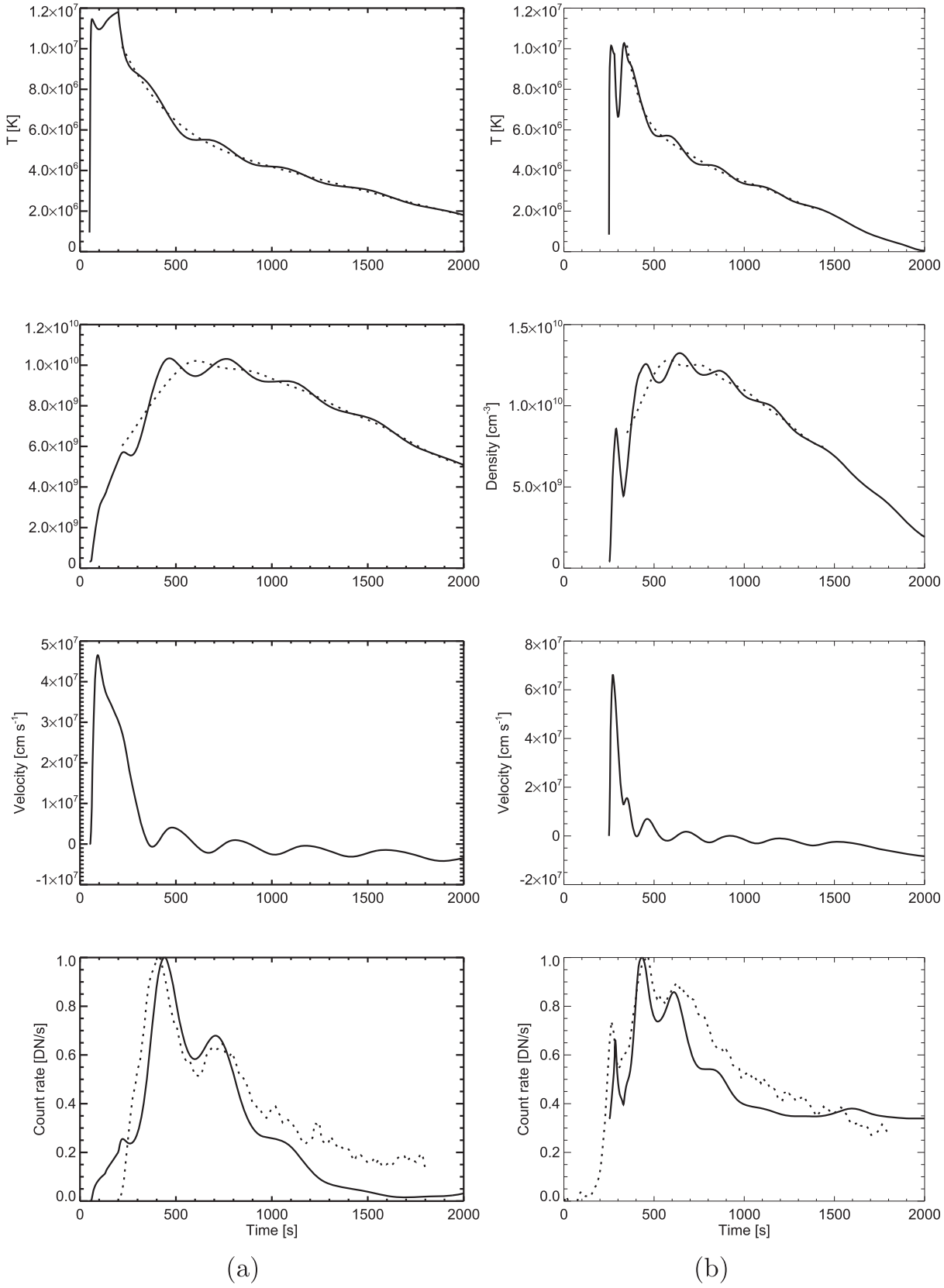

Figure 4. Results of hydrodynamic modeling of (a) a coronal loop heated with a pulse deposited uniformly in the loop and (b) a shorter loop heated with a pulse deposited at the footpoints (see the text for details): from top to bottom, evolution of the average temperature, density, velocity, and normalized light curve (solid lines) synthesized in the AIA 94 Å channel in the low loop segment of 30 Mm (a) and 20 Mm (b), roughly corresponding to the loop leg enclosed in box A (a) and boxes B and C (b) of Figure 1. The trends of the temperature and density variations used for an estimate of γ are also shown (dashed lines). The normalized light curves of boxes A and B (dashed lines) in Figure 2 are also shown for comparison. An offset of ∼50% of the maximum emission has been added to the model light curve in (b).

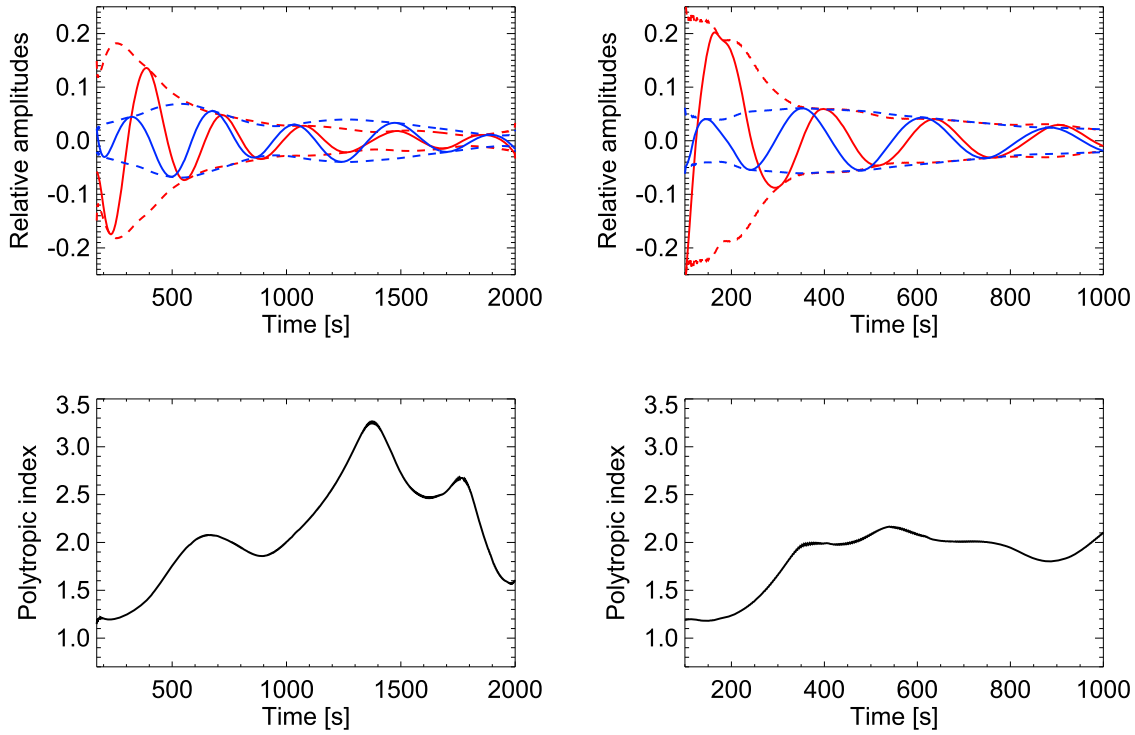

Figure 5. Top: relative temperature (blue) and density (red) variations, normalized to the corresponding trends $T_0(t)$ and $n_0(t)$ (for the model as on left-hand and right-hand sides as in Figure 4), and their instantaneous amplitudes $A_T(t)$ and $A_n(t)$ obtained using the Hilbert transform. Bottom: variation of the polytropic index with time, estimated from Equation (2).

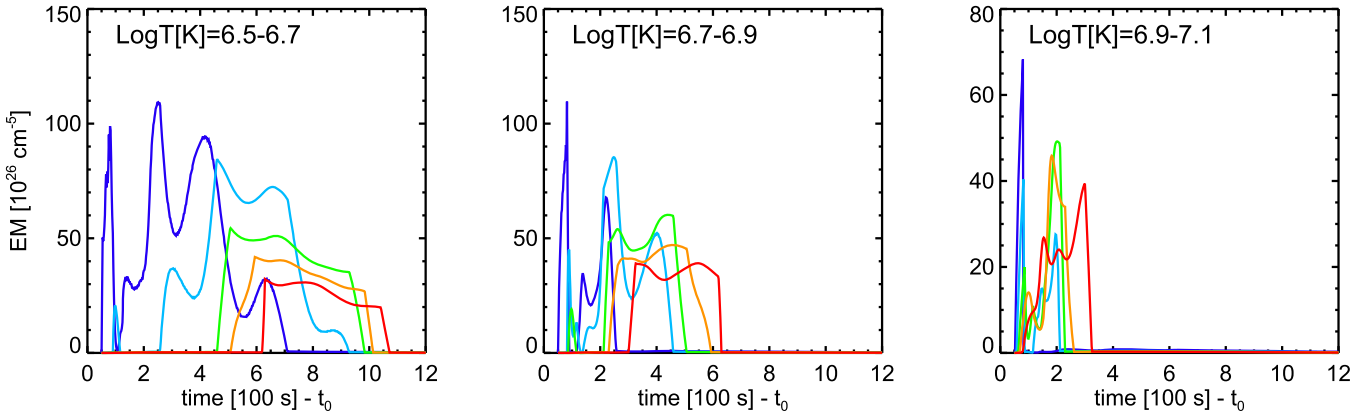

Figure 6. Emission measures vs. time for four segments along the model loop in Figure 4(b), respectively, in the same temperature bins as in Figure 3 for comparison. Time is shifted by $t_0 = 200$ s from that in Figure 4(b).

footpoints. We have ascertained that some important parameters of this simulation are quite well constrained: a heat pulse significantly longer than 30 s broadens the initial spike; a less intense pulse (half) produces a second pulsation much higher than the third one. The offset might indicate the presence of contributions from other transient components not included in our simple single loop model.

Finally, Figure 6 shows the evolution of the EM in the same temperature bins as in Figure 3 for four segments along the model loop with footpoint heating (Figure 4(b)). A comparison with Figure 4(b) shows a good qualitative agreement for the central temperature bin 6.7–6.9 $\log T$[K], and in particular regarding the timing of the peaks, and of the relative height of the peaks, except for the red curve as expected (Section 2.1). The coolest temperature bin is not directly comparable because in the observed one the background contribution is substantial. In the hottest bin, although the timing of the segments is the same, the timescale of the model evolution appear significantly shorter than the observed one. The comparison in this bin confirms that other hot components are probably present and our model cannot account for a multithermal structure across the loop.

3. Discussion

In this work we show the detection of quasiperiodic large-amplitude pulsations during transient and hot brightenings of a coronal loop system. The pulsations are detected in the legs of two distinct loops that intersect each other along the line of sight, and their amplitude is a large fraction ($\gtrsim$20%) of the total signal. This loop system is one of those where *IRIS* observed a hot spot in the UV Si IV 1402 Å line (Testa et al. 2019, in preparation) and where the related Doppler shift could be

explained only with a heat pulse driven by a nonthermal electron beam (Testa et al. 2014; Polito et al. 2018). The pulsations have been modeled caused by slow magnetoacoustic wave fronts moving along closed magnetic channels (Reale 2016) which can only occur with a short (∼1 minute) heat pulse (Equation (1)). Thus the observed QPP confirms the impulsive nature of the heating in this loop system, and even provides constraints on its duration.

We performed hydrodynamic modeling of coronal loops with impulsive heating that is able to reproduce the most important features of the quasiperiodic pattern, i.e., the amplitude and the period, together with the shape of the light curve and of the oscillation. The model does not fit the observation in all the details, but this is rarely the case for any detailed time-dependent modeling. We cannot exclude that other explanations are possible, but our results are obtained with a simple assumption on heating in a single closed loop, and are consistent with other independent evidence. As described in Reale (2016) the short heat pulse produces a pressure imbalance that drives a strong nonlinear pressure front traveling along the loop and reflecting against the twin front from the other leg at the loop top. A low-order standing mode settles inside the magnetic tube which acts as a wave guide. The wave propagation is purely hydrodynamic, so we cannot account for finite plasma-β and different MHD regimes (Nakariakov et al. 2017). The compressive wave fronts propagate approximately at the sound speed, and can therefore be interpreted in the more general framework of the slow magnetosonic waves (Nakariakov & Verwichte 2005; Kumar et al. 2013, 2015; Wang et al. 2015).

Our model is the same as those used in many other loop studies, including efficient thermal conduction (Spitzer 1962), in broad agreement with other wave spectroscopic (Van Doorsselaere et al. 2011) and imaging (Krishna Prasad et al. 2018) observations which found a polytropic index $\gamma \approx 1$, although a larger value was found in a flare observation (Wang et al. 2015).

The observed and modeled light curves (Figures 4) show a good agreement, including the fact that the AIA 94 Å channel detects only the hottest part of the loop's evolution, i.e., the event peak and initial cooling, and the related initial oscillation periods, after which the plasma exits the range of temperature sensitivity of the channel. The detection of more pulsation periods would be more appropriate to address other issues on longer timescales, such as wave damping (Ofman & Wang 2002; De Moortel & Hood 2003; Kumar et al. 2016).

We remark also that our loop model makes only a simple assumption on the impulsive heating function. Moreover, it includes a realistic transition region and chromosphere, and therefore the waves are not reflected at the lower boundary because of reflection boundary conditions but because they hit against the transition region.

Our model assumes that the loops are symmetric with respect to their apex (Peres et al. 1982). This assumption looks reasonable because both footpoints of both loops are observed to brighten (Figure 1). The slight asymmetries between the light curves of boxes B and C in Figure 2 are probably due to slight differences in the heating deposition, which we do not address here. We also point out that the loop lengths estimated from the observation do not match the loop lengths assumed in the modeling. Although the measured values represented the starting point for modeling, the best model lengths are fine-tuned directly from forward modeling until a good match of the light curves is found, both regarding the timescales, and in particular the decay time of the light curves, and the pulsation periods. The possible presence of magnetic twisting might explain why the measured lengths are smaller than the model lengths. According to Priest (2014), the ratio of the model to the observed length gives the twisting in units of 2 π. The resulting values of 1.3 and 1.6 do not look unreasonable.

The model provides us with useful physical insight and with important constraints. First, it is an independent check which confirms the interpretation given for *IRIS* observations of UV hot spots (Testa et al. 2014, 2019, in preparation; Polito et al. 2018), and observed mass rapid variability observed with the high spatial resolution coronal imager Hi-C (Testa et al. 2013). As mentioned above, the combination of density pulsations and rapid cooling shown in the first two rows of Figures 4 determines the emission evolution in the bottom panels, and we see only a couple of well-defined pulsations, because of the narrow temperature sensitivity of the AIA 94 Å channel (see Reale 2016 for more details).

The fine details of the observation allow us to push the model to constrain the location of the heat pulses inside the closed loops. We find that the pulsation sequence of the loop structure whose footpoint at the footpoint of which *IRIS* Doppler shifted spectra are observed includes a spike that is well explained if the heat pulse is located at the loop footpoints. This is probably consistent with the presence of nonthermal electron beams generated from reconnection of interacting magnetic structures and hitting the chromosphere at the footpoints. The duration of the heating is typically not easily constrained for impulsive events (e.g., Peres et al. 1987; Reale et al. 2000; Klimchuk 2006), but in this case the model constrains the duration of the heat pulse to be around 30 s, in agreement with estimates derived from the modeling of the *IRIS* brightenings (Testa et al. 2019, in preparation). Also the intensity of the heating is usually largely unknown but in this case we find that 10^{10} erg cm^{-2} s^{-1} is probably a very good reference value. The loop footpoint brightenings are short-lived ($\leqslant$1 minute) in the AIA 1600 Å channel (Figure 1(c)), which is consistent with the short duration of the heat pulse (e.g., Qiu et al. 2012; Testa et al. 2014).

The EM reconstruction along the loop confirms the presence of the pulsations at high temperature ($\log T[\mathrm{K}] \gtrsim 6.7$). In the limits of a single loop model which cannot account for thermal structuring across the loop, and for the brightening of other nearby structures, the model is able to reproduce the correct timing of the pulsations in the hot temperature bins and the details of them in the 6.7–6.9 $\log T$ [K] one, where the bulk of the brightening occurs (Figure 6). The high background probably prevents the detection of pulsations expected at later times at lower temperatures. In Figure 3(b) the first pulsation shifts by about 100 s from the leftmost to the third rightward point. This effect is probably real and marks the motion of the sloshing front. We measure an apparent speed of ∼75 km s^{-1}. We see the loop projected on the disk and if we correct for the estimated real loop curvature we obtain a true speed of ∼200 km s^{-1}, which becomes ∼320 km s^{-1} if we include twisting factor (1.6). If we assume that the front moves at the average (isothermal) sound speed $c_s \sim 0.11\, T^{1/2}$ km s^{-1} we obtain a temperature of ∼8 MK, quite consistent with the loop model.

The pulsations in another (and longer) loop structure show some qualitative difference (no spike) and allow us to constrain that the heat pulse is probably deposited higher in the corona. This loop structure is transverse to, and probably interacting with, the other. The efficient thermal conduction in the corona makes it difficult to constrain the location more in this case (e.g., Reale et al. 2000), any location will produce similar results there. We have a constraint of the pulse duration which is longer in this case, about 2.5 minutes.

We find then that in the same event we have heating deposited at loop footpoints and in the corona, with a duration of 0.5 and 2.5 minutes, respectively. This difference of heating location and duration in two nearby (probably interacting) structures within the same event broadens the scenario of impulsive heating deposition, and may have important implications within the framework of large-scale magnetic rearrangements and for the whole coronal heating theory.

In the end, the pulsations detected here are very strong evidence of the presence of impulsive heating inside a coronal loop system, similar to studies of Doppler loop oscillations observed by *SOHO*/SUMER (Wang et al. 2005). The predicted very high (to several hundreds km s^{-1}), hot but short-lived blueshifts coming up from the chromosphere at the very beginning of the loop brightening shifts might be detected by future EUV spectrometers and support further impulsive energy releases in active regions.

F.R. and A.P. acknowledge support from Italian Ministero dell'Istruzione, dell'Università e della Ricerca. P.T. acknowledges support by NASA grants NNX15AF50G and NNX15AF47G, and by contracts 8100002705 and SP02H1701R from Lockheed-Martin to SAO. D.Y.K. acknowledges support by the STFC consolidated grant ST/P000320/1. The authors thank the International Space Science Institute (ISSI) for their support and hospitality during the meetings of the ISSI team New Diagnostics of Particle Acceleration in Solar Coronal Nanoflares from Chromospheric Observations and Modeling.

ORCID iDs

Fabio Reale https://orcid.org/0000-0002-1820-4824
Paola Testa https://orcid.org/0000-0002-0405-0668
Dmitrii Y. Kolotkov https://orcid.org/0000-0002-0687-6172

References

Betta, R., Peres, G., Reale, F., & Serio, S. 1997, A&AS, 122, 585
Boerner, P. F., Testa, P., Warren, H., Weber, M. A., & Schrijver, C. J. 2014, SoPh, 289, 2377
Bradshaw, S. J., & Cargill, P. J. 2010, ApJ, 717, 163
Bradshaw, S. J., & Cargill, P. J. 2013, ApJ, 770, 12
Cargill, P. J., Warren, H. P., & Bradshaw, S. J. 2015, RSPTA, 373, 20140260
Cheung, M. C. M., Boerner, P., Schrijver, C. J., et al. 2015, ApJ, 807, 143
Cho, I.-H., Cho, K.-S., Nakariakov, V. M., Kim, S., & Kumar, P. 2016, ApJ, 830, 110
De Moortel, I., & Hood, A. W. 2003, A&A, 408, 755
De Moortel, I., & Hood, A. W. 2004, A&A, 415, 705
De Moortel, I., Hood, A. W., Gerrard, C. L., & Brooks, S. J. 2004, A&A, 425, 741
De Moortel, I., & Nakariakov, V. M. 2012, RSPTA, 370, 3193
Doyle, J. G., Shetye, J., Antonova, A. E., et al. 2018, MNRAS, 475, 2842
Fang, X., Yuan, D., Van Doorsselaere, T., Keppens, R., & Xia, C. 2015, ApJ, 813, 33
Goedbloed, J. P. H., & Poedts, S. 2004, Principles of Magnetohydrodynamics (Cambridge: Cambridge Univ. Press)
Hood, A. W., Browning, P. K., & van der Linden, R. A. M. 2009, A&A, 506, 913
Inglis, A. R., Ireland, J., Dennis, B. R., Hayes, L., & Gallagher, P. 2016, ApJ, 833, 284
Ionson, J. 1978, ApJ, 226, 650
Kim, S., Nakariakov, V. M., & Shibasaki, K. 2012, ApJL, 756, L36
Kliem, B., Karlický, M., & Benz, A. O. 2000, A&A, 360, 715
Klimchuk, J. 2006, SoPh, 234, 41
Kolotkov, D. Y., Pugh, C. E., Broomhall, A.-M., & Nakariakov, V. M. 2018, ApJL, 858, L3
Kopp, R., & Poletto, G. 1993, ApJ, 418, 496
Krishna Prasad, S., Raes, J. O., Van Doorsselaere, T., Magyar, N., & Jess, D. B. 2018, ApJ, 868, 149
Kumar, P., Innes, D. E., & Inhester, B. 2013, ApJL, 779, L7
Kumar, P., Nakariakov, V. M., & Cho, K.-S. 2015, ApJ, 804, 4
Kumar, S., Nakariakov, V. M., & Moon, Y. J. 2016, ApJ, 824, 8
Kupriyanova, E. G., Melnikov, V. F., Nakariakov, V. M., & Shibasaki, K. 2010, SoPh, 267, 329
Lemen, J. R., Title, A. M., Akin, D. J., et al. 2012, SoPh, 275, 17
McIntosh, S. W., De Pontieu, B., Carlsson, M., et al. 2011, Natur, 475, 477
McLaughlin, J. A., Hood, A. W., & de Moortel, I. 2011, SSRv, 158, 205
McLaughlin, J. A., Nakariakov, V. M., Dominique, M., Jelínek, P., & Takasao, S. 2018, SSRv, 214, 45
Morton, R. J., Weberg, M. J., & McLaughlin, J. A. 2019, NatAs, 3, 223
Murray, M. J., van Driel-Gesztelyi, L., & Baker, D. 2009, A&A, 494, 329
Nakariakov, V. M., Afanasyev, A. N., Kumar, S., & Moon, Y. J. 2017, ApJ, 849, 62
Nakariakov, V. M., Foullon, C., Verwichte, E., & Young, N. P. 2006, A&A, 452, 343
Nakariakov, V. M., Kosak, M. K., Kolotkov, D. Y., et al. 2019, ApJL, 874, L1
Nakariakov, V. M., & Melnikov, V. F. 2009, SSRv, 149, 119
Nakariakov, V. M., & Verwichte, E. 2005, LRSP, 2, 3
Ofman, L., Klimchuk, J., & Davila, J. 1998, ApJ, 493, 474
Ofman, L., & Wang, T. 2002, ApJL, 580, L85
Parker, E. 1988, ApJ, 330, 474
Peres, G., Reale, F., Serio, S., & Pallavicini, R. 1987, ApJ, 312, 895
Peres, G., Serio, S., Vaiana, G., & Rosner, R. 1982, ApJ, 252, 791
Polito, V., Testa, P., Allred, J., et al. 2018, ApJ, 856, 178
Priest, E. R. 2011, JASTP, 73, 271
Priest, E. R. 2014, Magnetohydrodynamics of the Sun (Cambridge: Cambridge Univ. Press)
Pugh, C. E., Armstrong, D. J., Nakariakov, V. M., & Broomhall, A.-M. 2016, MNRAS, 459, 3659
Qiu, J., Liu, W.-J., & Longcope, D. W. 2012, ApJ, 752, 124
Reale, F. 2014, LRSP, 11, 4
Reale, F. 2016, ApJL, 826, L20
Reale, F., Lopez-Santiago, J., Flaccomio, E., Petralia, A., & Sciortino, S. 2018, ApJ, 856, 51
Reale, F., Peres, G., Serio, S., et al. 2000, ApJ, 535, 423
Reale, F., Testa, P., Petralia, A., & Graham, D. 2019, ApJ, 882, 7
Ruderman, M. S. 2013, A&A, 553, A23
Selwa, M., Murawski, K., & Solanki, S. K. 2005, A&A, 436, 701
Simões, P. J. A., Hudson, H. S., & Fletcher, L. 2015, SoPh, 290, 3625
Spitzer, L. 1962, Interscience Tracts on Physics and Astronomy, Vol. 3, Physics of Fully Ionized Gases (2nd ed.; New York: Interscience)
Svestka, Z. 1994, SoPh, 152, 505
Testa, P., De Pontieu, B., Allred, J., et al. 2014, Sci, 346, 1255724
Testa, P., De Pontieu, B., Martínez-Sykora, J., et al. 2013, ApJL, 770, L1
Testa, P., & Reale, F. 2012, ApJL, 750, L10
Thurgood, J. O., Pontin, D. I., & McLaughlin, J. A. 2019, A&A, 621, A106
van Ballegooijen, A. A., Asgari-Targhi, M., Cranmer, S. R., & DeLuca, E. E. 2011, ApJ, 736, 3
Van Doorsselaere, T., Kupriyanova, E. G., & Yuan, D. 2016, SoPh, 291, 3143
Van Doorsselaere, T., Wardle, N., Del Zanna, G., et al. 2011, ApJL, 727, L32
Vekstein, G., & Katsukawa, Y. 2000, ApJ, 541, 1096
Verwichte, E., Haynes, M., Arber, T. D., & Brady, C. S. 2008, ApJ, 685, 1286
Wang, T. 2011, SSRv, 158, 397
Wang, T., Ofman, L., & Davila, J. M. 2013, ApJL, 775, L23
Wang, T., Ofman, L., Sun, X., Provornikova, E., & Davila, J. M. 2015, ApJL, 811, L13
Wang, T., Ofman, L., Sun, X., Solanki, S. K., & Davila, J. M. 2018, ApJ, 860, 107
Wang, T. J., Solanki, S. K., Innes, D. E., & Curdt, W. 2005, A&A, 435, 753
Zavershinskii, D. I., Kolotkov, D. Y., Nakariakov, V. M., Molevich, N. E., & Ryashchikov, D. S. 2019, arXiv:1907.08168